1-2019

Structure and Growth of Core–shell Nanoprecipitates in Al–Er–Sc–Zr–V–Si High-temperature Alloys

Wahaz Nasim

Saegh Yazdi

Ruben Santamarta

Jahanzaib Malik

Dinc Erdeniz

See next page for additional authors

Authors

Wahaz Nasim, Saegh Yazdi, Ruben Santamarta, Jahanzaib Malik, Dinc Erdeniz, Bilal Mansoor, David N. Seidman, David C. Dunand, and Ibrahim Karaman

Structure and Growth of Core–shell Nanoprecipitates in Al–Er–Sc–Zr–V–Si High-temperature Alloys

Wahaz Nasim
Department of Materials Science and Engineering, Texas A&M University, College Station, TX
Sadegh Yazdi
Renewable and Sustainable Energy Institute, University of Colorado Boulder, Boulder, CO
Ruben Santamarta
Departament de Fisica, Universitat de les Illes Balears, 07122 Palma de Mallorca, Spain
Jahanzaib Malik
Department of Materials Science and Engineering, Texas A&M University, College Station, TX
Dinc Erdeniz
Department of Materials Science and Engineering, Northwestern University, Evanston, IL
Bilal Mansoor
Department of Materials Science and Engineering, Texas A&M University, College Station, TX
Mechanical Engineering Program, Texas A&M University at Qatar, Education City, Doha, Qatar
David N. Seidman

Department of Materials Science and Engineering, Northwestern University, Evanston, IL
NanoAl LLC, 8025 Lamon Ave Suite 446, Skokie, IL
Northwestern University, Center for Atom-Probe Tomography (NUCAPT), 2220 Campus Drive, Evanston, IL
David C. Dunand
Department of Materials Science and Engineering, Northwestern University, Evanston, IL
NanoAl LLC, 8025 Lamon Ave Suite 446, Skokie, IL
Ibrahim Karaman
Department of Materials Science and Engineering, Texas A&M University, College Station, TX

ABSTRACT

Lightweight Sc-containing aluminum alloys exhibit superior mechanical performance at high temperatures due to core–shell, $L1_2$-ordered trialuminide nanoprecipitates. In this study, the structure of these nanoprecipitates was studied, using different transmission electron microscopy (TEM) techniques, for an Al–Er– Sc–Zr–V–Si alloy that was subjected to a two-stage overaging heat treatment. Energy-dispersive X-ray spectroscopy of the spherical Al_3(Sc, Zr, Er ,V) nanoprecipitates revealed a core–shell structure with an Sc- and Er-enriched core and a Zr-enriched shell, without a clear V outer shell. This structure is stable up to 72% of the absolute melting temperature of Al for extended periods of time. High-angle annular dark-field scanning TEM was used to image the {100} planes of the nanoprecipitates, demonstrating a homogeneous $L1_2$-ordered superlattice structure for the entire nanoprecipitates, despite the variations in the concentrations of solute atoms within the unit cells. A possible growth path and compositional trajectory for these nanoprecipitates was proposed using high-resolution TEM observations, where different rod-like structural defects were detected, which are considered to be precursors to the spherical $L1_2$-ordered nanoprecipitates. It is also hypothesized that the structural defects could consist of segregated Si; however, this was not possible to verify with HAADF-STEM because of the small differences in Al and Si atomic numbers. The results herein allow a better understanding of how the Al–Sc alloys' core–shell nanoprecipitates form and evolve temporally, thereby providing a better physical picture for future atomistic structural mappings and simulations.

Introduction

Aluminum alloys that are mechanically functional at high temperatures ([0.5 Tm) are in high demand in aerospace, automotive and power transmission industries. These applications require alloys with high specific strength, high electrical conductivity, good oxidation resistance, high creep properties, good coarsening resistance of the strengthening nanoprecipitates, low cost and low density. The mechanical strength of commercial Al alloys deteriorates at temperatures above ~ 200 to 250 ^{o}C due to either dissolution or coarsening of the nanoprecipitates, which provide high-temperature strength. Hence, rigorous precipitate design approaches have recently been considered for the next generation of high-temperature Al alloy grades [1–11].

Aluminum alloys micro-alloyed with scandium are promising candidates for high-temperature applications since they demonstrate good mechanical properties at temperatures to at least ~ 300 ^{o}C, as a result of Al_3Sc ($L1_2$) nanoprecipitates [1–4]. $L1_2$-ordered Al_3Sc nanoprecipitates, with diameters greater than a few nanometers, are known to pin grain boundaries (GBs) (thereby maintaining fine grain sizes at high temperatures), while retaining Orowan dislocation looping mechanisms at ambient and high temperatures [3]. In the past decade, Al–Sc alloys micro-alloyed with Zr have exhibited slower nanoprecipitate coarsening kinetics, which further extends the use of these alloys at temperatures as high as ~ 400 ^{o}C [5–8]; this corresponds to 72% of the absolute melting temperature of Al. Furthermore, Er (and other lanthanoids) can replace some of the Sc in the nanoprecipitates

and create an Al_3(Er, Sc) core with a larger lattice parameter mismatch between the nanoprecipitates and the Al (f.c.c.) matrix, consequently very effectively decreasing dislocation creep at high temperatures [6, 9].

Adding rare-earth elements with different diffusivities was proposed in later renderings of this alloy to create core–shell nanoprecipitates with a layered structure [6, 7, 9, 10]. Erbium microalloying of Al–Sc and Al–Er–Zr alloys uses the diffusivity differences among Er, Sc and Zr in Al to create a core–shell nanoprecipitate structure, forming nanoonion-type structures [6, 10]. In the ternary and quaternary systems with Al_3(Sc, Zr, Er) nanoprecipitates, the core is Er rich, the inner-shell is Sc rich and the outer shell is Zr rich. The slower diffusing Zr-rich outer shell encapsulates the faster diffusing elements in the inner-core, thereby decelerating the coarsening kinetics, which results in stable and mechanically functional materials at temperatures as elevated as 400 C [5, 8, 10]. $L1_2$-ordering is maintained for all layers of these core–shell nanoprecipitates for extended periods of time, which ensures a coherent interface between the matrix and nanoprecipitates.

Recently developed Al–Er–Sc–Zr–V–Si alloys, with a V-enriched outermost shell, display a stable Vickers microhardness of ~ 450 MPa after exposure to temperatures as high as 400 ^{o}C [10]. This high microhardness is achieved via a two-stage aging process: first aging at 350 ^{o}C permits the high-diffusivity elements (Er and Sc) to form the inner part of the precipitate core; subsequent aging at 400 C allows the slower diffusing elements (Zr and V) to form shells enveloping the Er- and Sc-enriched core. While atomprobe tomography (APT) has been recently used to study these nanoprecipitates [10, 12, 13], to the best of our knowledge, there are not detailed studies using high-resolution transmission electron microscopy (HRTEM) for imaging these nanoprecipitates, thereby, revealing their core–shell structure.

Al_3Sc nanoprecipitates have a faceted morphology during growth, and the number of {hkl} facets depends on the aging temperature and time [3]. Studying the temporal evolution of Al_3(Sc, Zr) nanoprecipitates in alloys aged at 300 ^{o}C yields a similar facetted structure [4, 14–17]. However, the morphology of the compositionally complex nanoprecipitates in Al–Er–Sc–Zr–V–Si alloys has not been reported in detail to date. The crystal structure of Al_3(Sc, Zr, Er, V) nanoprecipitates is likely to be similar to that of Al_3(Sc, Zr) nanoprecipitates, but there are no reports on the superlattice mapping of these nanoprecipitates. A knowledge of the exact superlattice structure is important for molecular dynamic simulations or binding-energy calculations for creating optimal core–shell nanoprecipitates in future high-temperature aluminum alloys.

To shed light on the evolution of these nanoprecipitates in Al–Sc-based alloys, crystal imperfections need to be studied using atomic resolution techniques such as HRTEM and high-resolution scanning transmission electron microscopy (HRSTEM). For example, the formation of Cu clusters in naturally aged Al-Cu alloys was demonstrated to be the precursor to GP-zones using HRTEM [18]. HRTEM was utilized to discover GP(II) zones in Al-Zn-Mg alloys, composed of only a few atomic layers, 3–5 nm thick [19]. The atomic distortions in the lattice caused by such GP(II) zones were distinctly observed utilizing HRTEM. The Zn-rich GP(II)-zones were determined to be precursors to the fully developed g-precipitates, $MgZn_2$, in Al–Zn–Mg alloys [19]. In later renditions of Al–Zn–Mg alloys, additions of Sc and Zr resulted in Al_3(Sc, Zr) nanoprecipitates, with Al–Zn–Mg η’ - precipitates remaining in the matrix [20]. These examples demonstrate the power of HRTEM for understanding the temporal evolution of nanoprecipitates and how their crystal structures can be differentiated in different phases of growth in aluminum alloys.

Herein, similar techniques were employed for Al_3(Sc, Zr, Er, V) nanoprecipitates in Al–Er–Sc–Zr–V– Si alloys to reveal in detail their nanostructure and shed light on the growth mechanisms of core–shell nanoprecipitates. Specifically, the structure of nanoprecipitates in an Al–0.005Er–0.02Sc–0.07Zr–0.08V– 0.06Si (at%) alloy was studied using HRTEM and HRSTEM, after an overaging heat treatment (350 ^{o}C for 16 h and 450 ^{o}C for 24 h), which was utilized to create core–shell nanoprecipitates [10]. Additionally, HRTEM and differential scanning calorimetry (DSC) measurements on the initial homogenized material were used to check the possibility of the

formation of clusters and GP-zones. HRTEM was also employed to follow the growth of structural defects/atomic clusters into GP-zones, and subsequently to spherical nanoprecipitates in the overaged samples.

Materials and methods

Material fabrication and heat treatments

The alloy, with a nominal composition of Al–0.005Er– 0.02Sc–0.07Zr–0.08V–0.06Si (at%), was prepared using 99.99% pure Al and master alloys of Al5.9 wt% Er, Al-2 wt% Sc, Al-8 wt% Zr, Al-5 wt% V and Al-12.6 wt% Si. All the pieces were melted in alumina crucibles at 800 ^{o}C in a resistively heated muffle furnace and stirred five times using alumina rods with a 15-min hold time between each stir. Subsequently, the samples were cast in graphite molds, which were preheated to 200 ^{o}C and then placed on an ice-cooled copper platen to promote directional solidification. Upon full solidification, which takes 20–30 s, the ingots were quenched into an iced water bath. Then, a homogenization treatment was performed at 640 ^{o}C for 4 h. Additionally, one of the homogenized samples was aged at a primary aging temperature of 350 ^{o}C for 16 h and a secondary aging temperature of 450 ^{o}C for 24 h. These heat treatments and casting methods were utilized in Ref. [10] to develop core–shell nanoprecipitates in an Al–Er–Sc–Zr–V–Si alloy. The two sets of samples used in the present experiments will be referred to as homogenized and overaged Al alloys.

Precipitate characterization

Transmission electron microscopy (TEM) specimens were prepared by cutting ~ 1.5 mm thick samples with a diamond saw, followed by mechanical grinding with SiC paper to a thickness of ~ 70 μm. Standard 3 mm TEM disks were mechanically punched from the thin foils and twin-jet electropolished, employing a 30 vol% nitric acid and 70 vol% methanol electrolyte solution at - 10 ^{o}C. A 10-V DC potential was utilized at a current of 70–90 mA. Immediately after twin-jet electropolishing, the specimens were cleaned utilizing three different methanol baths. TEM and HRTEM images were acquired employing an FEI Tecnai G2 F20 ST. Energy-dispersive X-ray spectroscopy (EDS) and high-resolution high-angle annular dark-field (HAADF) STEM analyses were performed at 200 kV in a double Cs corrected FEI Titan Themis Cubed STEM, equipped with a Super-X quad EDS detector. The probe semi-angle, and the inner and the outer collection angles were set at 30 mrad, 65 mrad and 200 mrad, respectively. The hkl diffraction spots from the TEM analyses were indexed using CaRIne Crystallography (CaRIne Crystallography, Senlis, France) and JEMS (Interdisciplinary Center for Electron Microscopy, Swiss Federal Institute of Technology Lausanne) software.

Differential scanning calorimetry

Differential scanning calorimetry (DSC) experiments were performed using a LabsysTM TG-DSC, manufactured by SETARAM, to reveal the evolution of the nanoprecipitates. The DSC specimens were cut from the center of the homogenized billet and then ground to a mass of 25 mg. The specimen was weighed using a Semi Micro Balance CX205, with an accuracy of ± 0.03 mg. Before the scan, a specimen was equilibrated at 25 ^{o}C for 5 min using a nitrogen flow rate of 20 ml/min. The scan was then performed using a heating rate of 20 ^{o}C/min up to 600 C. An empty pan DSC run was performed to make a baseline correction. A multi-peak fitting analysis employing IGOR software was utilized to remove the background noise.

Results and discussions

The microstructure and the effects of the heat treatments on the cast alloy were reported earlier [10]. Direct-current plasma-atomic emission spectroscopy (DCP-AES) and APT were performed to confirm the nominal composition of the alloy, Al–0.007Er– 0.013Sc–0.071Zr–0.074V–0.054Si (at%). Except for a leaner Sc content, the concentrations of all the other elements were close to the nominal values.

Atomic structure of spherical precipitates

Overaged Al–Er–Sc–Zr–V–Si samples were studied using TEM to determine the atomic structure and measure the composition of the nanoprecipitates. Figure 1a displays a dark-field TEM image of the spherical nanoprecipitates, which are uniformly distributed throughout the Al (f.c.c.) matrix. The diameter of the nanoprecipitates ranges from ~ 0.7 to 17 nm with an average diameter of 7.1 ± 3.4 nm. These values were confirmed using measurements taken on other TEM images, not shown here.

Figure 1b shows a diffraction pattern along the [110] zone axis of a small collection of nanoprecipitates. The fundamental hkl spots (labeled in white) indicate the f.c.c. structure of the aluminum matrix, while the superlattice hkl spots (labeled in orange) indicate the $L1_2$ unit cell structure of the nanoprecipitates. In Fig. 1b, the $L1_2$ superlattice hkl spots are located at the midway positions between the fundamental hkl spots, which demonstrate the lattice parameter of the nanoprecipitates is similar to that of the Al matrix, 4.05 A˚.

To further confirm the crystal structure, STEM-EDS and atomic resolution HAADF-STEM experiments were conducted on multiple spherical nanoprecipitates. Figure 2 shows STEM-EDS elemental maps of one of these spherical nanoprecipitates. The elemental EDS maps display a core–shell precipitate structure within the Al matrix. The faster diffusing elements, Er and Sc, are enriched in the core, while the slower diffusing element, Zr, forms an outer shell. The diffusivities of each element within Al (f.c.c.) were reported to be 6.4×10^{-24} [21], 9×10^{-20} [22], and 4×10^{-19} m^2 /s [23] for Zr, Sc and Er, respectively, at a temperature of 300 ^oC [24]. The activation energy for the diffusion of V in Al is even higher than that of Zr [25]. This particular EDS map suggests that V is distributed almost uniformly and is not concentrated in an outermost shell. EDS measurements of Si were performed within the nanoprecipitate and f.c.c. matrix, resulting in equal intensity levels for both cases; hence, Si was excluded from this analysis. The lack of a V shell is due to the segregation of eutectic elements (Er and Sc) into the dendrite channels and peritectic elements (Zr and V) into the dendrite cores. The presence of a strong signal from Er and Sc, forming the core of the precipitate, suggests that this particular specimen was sampled from a dendritic channel rich in Er and Sc, but poor in Zr and V. Due to the strong partitioning behavior of Zr to the precipitates, a clear Zr-enriched shell is still present, despite the lower overall Zr concentration; however, as V weakly partitions into the precipitate, little V is found in the precipitates.

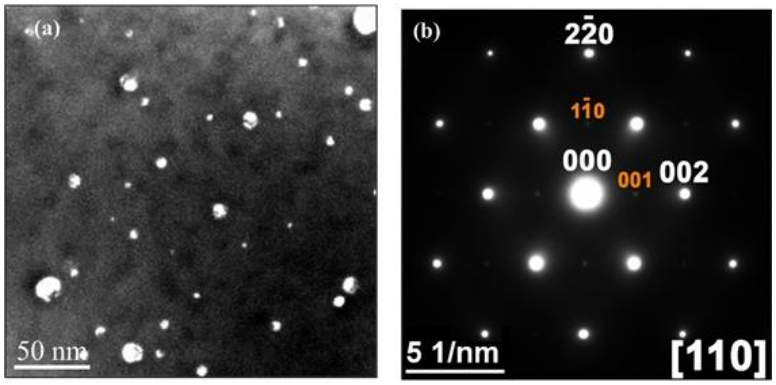

Figure 1 a Dark-field TEM image of Al_3(Sc, Zr, Er, V) spherical nanoprecipitates in an Al (f.c.c.) matrix; and b corresponding diffraction pattern of a distribution of nanoprecipitates recorded along the [110] zone axis where the f.c.c. diffraction spots are labeled in white and the $L1_2$ diffraction spots from the nanoprecipitates are labeled in orange.

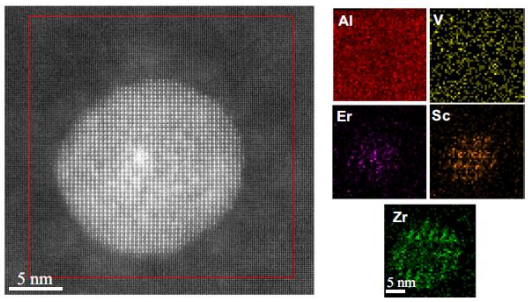

Figure 2 A HAADF-STEM image of a Al_3(Sc, Zr, Er, V) spherical nanoprecipitate with its associated elemental EDS maps for Al, V, Er, Sc and Zr, exhibiting the core–shell morphology of the nanoprecipitate with an Er-rich area at the core, followed by Sc and Zr shells. A visible V layer was not distinguishable.

To calculate the volume fractions of the Er-, Sc- and Zr-enriched shells, the EDS maps of five nanoprecipitates, with diameters ranging from 12 to 20 nm, were utilized, assuming perfect spherical morphologies and excluding overlapping elemental regions. As a result, the volume fractions of Er-, Sc- and Zr-rich core and shells are determined to be 0.13 ± 0.03, 0.16 ± 0.12 and 0.71 ± 0.13, respectively, making these nanoprecipitates overall Zr rich. Erdeniz et al. [10] obtained similar nanoprecipitate core–shell structures using APT for the same alloy with the same heat treatments. In some locations, the nanoprecipitates lack a V (Z = 23) shell, which is attributed to elemental macrosegregation caused by dendritic solidification of the cast alloy. APT of a nanoprecipitate in a completely different location in the alloy displayed, however, a V-containing Zr-rich shell [10].

Figure 3 shows an atomic resolution HAADFSTEM image of a core–shell spherical nanoprecipitate recorded along the [100] direction. The HAADF signal from each atomic column is proportional to $Z^{1.7}$ (Z = atomic number) and therefore reflects the difference in atomic numbers of different species within the columns [26]. The higher contrast regions depict a spherical nanoprecipitate, and the low-contrast region is the Al matrix. Near the matrix/nanoprecipitate heterophase interface, there is a drastic increase in contrast caused by the heavier atomic masses of V- and Zr-enriched regions. Further toward the central core of the nanoprecipitate, the contrast increases further where the Sc- and Er-enriched regions are located. The facets associated with the {110} and {100}-planes are observed in Figs. 2 and 3 for these complex nanoprecipitates, which are also found in the Al–Sc binary system containing Al_3Sc nanoprecipitates in an Al matrix [6, 14–17].

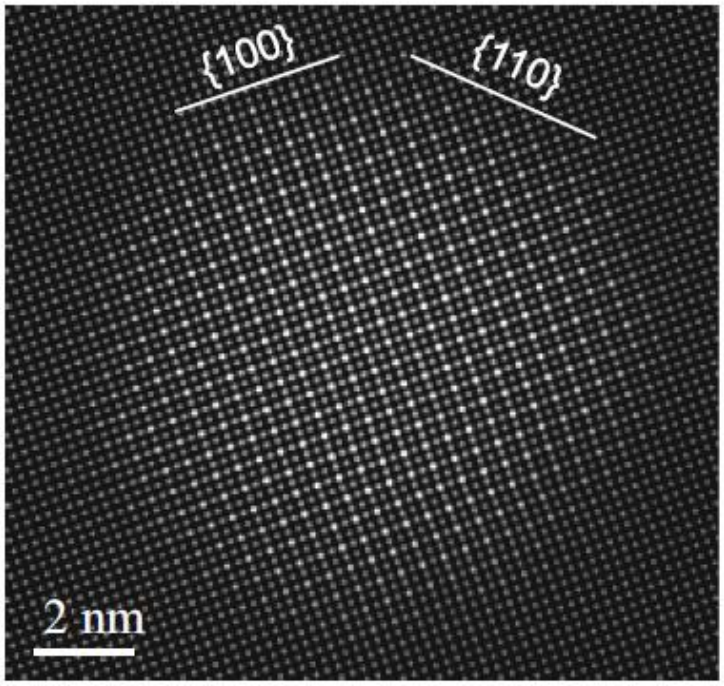

Figure 3 HAADF-STEM image of an Al_3(Sc, Zr, Er, V) spherical nanoprecipitate recorded along the [100] direction, (100) plane, displaying a contrast difference between the nanoprecipitate and the pure Al (f.c.c.) matrix.

Figure 4a displays a HAADF-STEM image of a spherical nanoprecipitate recorded along the [100] direction, with two marked lines on two adjacent rows of atoms, N1 and N2, traversing the pure Al matrix, through the entire diameter of the nanoprecipitate, and into the other side of the Al matrix. Figure 4b displays the line profile intensity plot for lines N1 and N2. Both lines display contrast peaks and troughs, where each peak indicates the position of an atomic column and each trough is free space between neighboring atomic columns. The N1 profile displays relatively similar contrast effects throughout the entire nanoprecipitate and matrix regions. This indicates that the specimen has a uniform thickness in this area and that the majority of the atoms in line N1 are Al atoms. The slight increase in the number of counts for line N1 in the nanoprecipitate region is a result of signal leaking from the neighboring heavier elements in line N2 due to dynamic elastic scattering [27]. Line N2 indicates a pure Al matrix; however, starting from the matrix/nanoprecipitate heterophase interface, there are alternating peaks of heavy and light elements, consistent with high-count peaks representing V (Z = 23), Zr (Z = 40), Sc (Z = 21) and Er (Z = 68) atoms and low-count peaks from Al (Z = 13) atoms. The core of the nanoprecipitate yields the highest count peaks, consistent with its Er (Z = 68) enrichment.

To accurately derive the exact structure of the nanoprecipitates, an additional HAADF-STEM image was analyzed further for the [100] direction. Figure 5a displays a magnified cross section of the nanoprecipitate, where the left- and right-hand regions are the Al matrix, and the center high-intensity region is the core–shell structure of the nanoprecipitate. Three rows, labeled 1, 2 and 3, containing the heavy elements V, Zr, Sc and Er were used to calculate the concentration ratio profiles displayed in Fig. 5b–d for each row, based on the integrated intensities at each atomic column, as described below. The Zr, Sc and Er concentration values on the y-axis of the concentration profiles in Fig. 5b–d have been offset by 1, 2 and 3 units of concentration for better graphical interpretation, so that all concentrations are with respect to their respective baselines. HAADF-STEM images are 2-D projection images; therefore, the contrast at each atomic position is the result of all the atoms within the column. The integrated intensity was measured for each atomic position, and it was normalized with respect to the average intensity of the four adjacent pure Al columns for every heavy element atomic position. This was

done to remove the bias due to the small variations in intensity observed in the line profile measurements in Fig. 4b.

The atomic number (Z) of each atomic position and thickness of the foil (t) was then related to the normalized integrated intensity (I) using Eq. (1) below [26].

$$I \propto Z^{1.7} * t \quad (1)$$

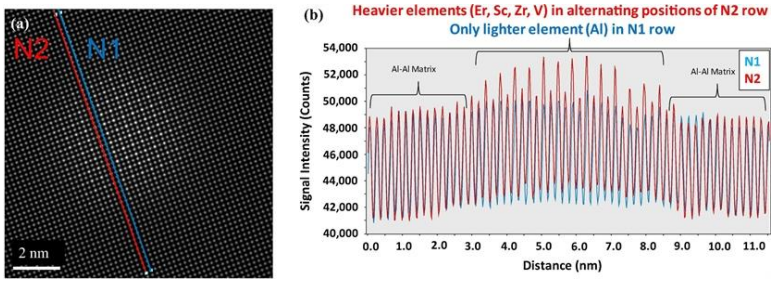

Figure 4 a HAADF-STEM image of a 6 nm diameter Al_3(Sc, Zr, Er, V) nanoprecipitate and b its corresponding intensity profiles along the face centered positions of two adjacent unit cells across the nanoprecipitate, N1 (blue) and N2 (red). The intensity profiles indicate only Al atoms in the N1 row, demonstrating almost a pure f.c.c. unit cell structure. N2 row has an alternating signal from Al and other heavier solute atoms confirming the $L1_2$-ordered structure of the second row.

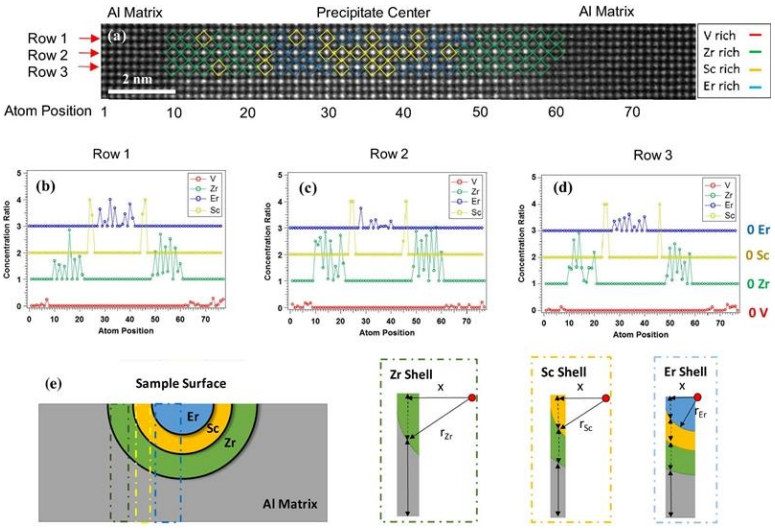

Figure 5 a HAADF-STEM image of a (100) plane nanoprecipitate cross section marked with their respective elemental rich atoms occupying the face centered positions of the unit cell. The line profiles of concentration ratios for the three rows containing heavy elements; b Row 1; c Row 2; and d Row 3. The Zr, Sc and Er concentration ratio profiles have been offset by 1, 2 and 3 units for the ease of representation. e The schematic represents the geometrical half-spherical precipitate assumption for calculating the atomic positions and line profiles of concentration ratios in a through d. See the text for details.

Silicon was removed from the analysis because its Z value (14) is only one unit different from that of Al (Z = 13); hence, the intensity difference is negligible. The intensity measurements of all three rows were averaged at the Al matrix positions (atomic positions 1–8 and 62–77 in Fig. 5a), and the atomic number was set to 13 for Al in Eq. (1).

Figure 5e shows a schematic of the precipitate structure within the Al matrix where half of the spherical precipitate was assumed to be sitting on the surface of the foil. A full precipitate assumption sitting within the matrix was also considered; however, this assumption resulted in higher background intensities than the measured intensity values, especially at the precipitate core, which resulted in negative concentration ratios within the precipitate. The nanoprecipitate in Fig. 5a was divided into three distinct elemental regions with sharp interfaces between each shell as shown in Fig. 5e (Zr, Sc and Er, without V since the EDS maps did not reveal V shell). Based on the average volume factions determined from the EDS maps mentioned earlier, the radius of the Zr shell of the precipitate in Fig. 5a was assumed to be from ~ 3 to 5 nm from the center of the precipitate. Similarly, the Sc shell was calculated to be ~ 2 to 3 nm thick and the central Er core was set to a 2-nm radius. These radii were only used as an initial assumption for calculating the intensities in the equations given below, and the true radii of these shells are derived below. In order to calculate the intensity from each pure elemental shell of the precipitate, as a function of position x, a geometrical factor using a concentric half-spherical precipitate was assumed. Figure 5e displays how the thickness of each shell changes as a function of position x along the precipitate and can be easily calculated using simple geometry. Equations 2 through 4 were then used to calculate the intensity contribution for each element (IZr, ISc and IEr) from the measured intensity (IMeasured) in Fig. 5a at a constrained radius interval. The intensity contribution of the Al matrix (IAl(x)) changes as a function of position x as shown in Fig. 5e which needs to be subtracted from the measured intensity and can be calculated with simple trigonometry rules and the radius of each shell.

$$I_{\mathrm{Zr}} = I_{\mathrm{Measured}} - I_{\mathrm{Al}}(x)\; r_{\mathrm{Zr}} > x > r_{\mathrm{Sc}} \quad (2)$$

$$I_{\mathrm{Sc}} = I_{\mathrm{Measured}} - \mathrm{Z}_{\mathrm{Zr}}^{1.7} * \left(\sqrt{r_{\mathrm{Zr}}^2 - x^2}\right) - I_{\mathrm{Al}}(x) \quad (3)$$
$$r_{\mathrm{Sc}} > x > r_{\mathrm{Er}}$$

$$I_{\mathrm{Er}} = I_{\mathrm{Measured}} - \left[\mathrm{Z}_{\mathrm{Zr}}^{1.7} * \left(\sqrt{r_{\mathrm{Zr}}^2 - x^2} - \sqrt{r_{\mathrm{Sc}}^2 - x^2}\right)\right] \quad (4)$$
$$-\mathrm{Z}_{Sc}^{1.7}\left(\sqrt{r_{\mathrm{Sc}}^2 - x^2}\right) - I_{\mathrm{Al}}(x)\; x < r_{\mathrm{Er}}$$

The intensities calculated from Eqs. 2–4 can then be normalized with respect to the ideal intensity of each shell, assuming that the shell only consists of a particular element, which is calculated using Eqs. 5–7. The normalized intensities demonstrate the concentration ratio of each atomic column or position shown in Fig. 5b–d, with respect to that particular element assigned to the specific shell. For the region outside the precipitate, the V concentration ratio was simply calculated to be the ratio of the intensity measured and the calculated Al matrix intensity.

$$I_{\mathrm{Zr,ideal}} \propto \mathrm{Z}_{\mathrm{Zr}}^{1.7} * \left(\sqrt{r_{\mathrm{Zr}}^2 - x^2}\right)\; r_{\mathrm{Zr}} > x > r_{\mathrm{Sc}} \quad (5)$$

$$I_{\mathrm{Sc,ideal}} \propto \mathrm{Z}_{\mathrm{Zr}}^{1.7} * \left(\sqrt{r_{\mathrm{Sc}}^2 - x^2}\right)\; r_{\mathrm{Sc}} > x > r_{\mathrm{Er}} \quad (6)$$

$$I_{\mathrm{Er,ideal}} \propto \mathrm{Z}_{\mathrm{Zr}}^{1.7} * \left(\sqrt{r_{\mathrm{Er}}^2 - x^2}\right)\; x > r_{\mathrm{Er}} \quad (7)$$

Figure 5a shows the concentration map of each element in the precipitate where each colored box represents the richest element in that particular atomic column in the precipitate. In the Zr shell, the atomic column with a concentration ratio of above 0.5 (50%) is marked with a green box showing that particular atomic position is Zr rich. A concentration ratio below 0.5 was going to be labeled V-rich with a red box; however, no V-rich region was observed in Fig. 5a. Furthermore, if the Zr concentration is below 0.5, closer to the core of the precipitate, the atomic column in the precipitate is assumed to be Sc rich, since the Sc and Zr regions may overlap. At the core of the precipitate, if a concentration ratio below 0.5 is observed for Er, then the atomic column at the core of the precipitate is assumed to be Sc rich as is observed in Fig. 2. Some negative concentration ratios were also calculated for the Al columns with this method, which was extrapolated to zero in Fig. 5b–d. This was probably due to the half-spherical precipitate assumption in the calculations. Regarding the nonlinear thickness effects on intensity, the precipitate was assumed to be sitting within the Al matrix. Under this assumption, since the precipitate size is smaller than 10–20 nm, nonlinear thickness effects are negligible and can be ignored in the calculations of concentration ratios [28].

It has to be noted that the above method only shows a simplified, first-order approach to calculate concentration ratios of each element within the nanoprecipitate and many geometrical, interface and diffraction assumptions have been made. The method could be improved by applying multislice simulation during the HRSTEM analysis.

Figure 5a does not display a V-rich shell at the matrix/nanoprecipitate heterophase interface, confirming EDS results in Fig. 2. This lack of an Al_3V layer is due to the dendritic macrosegregation during casting, creating local V depleted regions, as explained above. The exact thickness of the Zr-enriched shell varies between rows 1, 2 and 3 and is about ~ 3 nm with some atomic positions of low intensity suggesting Sc-rich regions within this shell. At the core of the precipitate, measuring about ~ 5 nm in diameter, rows 1 and 3 display a random distribution of Er and Sc-rich atomic positions; however, row 2 exhibits a Sc-rich region at the center. Clearly, there is a lack of a sharp transition between the Sc and Er core/shell. This was not anticipated, as a purely Er-rich region should have been observed at the center of the precipitate with a Sc-rich outer shell [10], based on the strong assumption that the tracer diffusivities of the elements in pure Al are relevant for non-ideal Al alloy solid-solution systems with highly correlated diffusion [29, 30]. To summarize the above observations, the core of the precipitate investigated in Fig. 5 is composed of a randomly distributed Sc- and Er-rich regions surrounded by a well-developed Zr shell.

The crystal structure of the precipitates is consistent with an $L1_2$-ordered structure, where two distinct parallel atomic planes can be distinguished. Examining the structure along a < 100 > direction, rows 1, 2 and 3 were found to alternate between Al and heavier atomic elements (Er, Sc, Zr and V), whereas the adjacent atomic planes exhibit a majority of Al atoms. Furthermore, the $L1_2$-ordered superlattice structure of the nanoprecipitates is maintained for the entire nanoprecipitates in spite of the different compositions of the shells, a feature not been confirmed using HRTEM. It is likely that this structure holds for other Al–Sc-based alloys, but additional compositions need to be analyzed to confirm this hypothesis.

Figure 6 displays a HAADF-STEM image and atomic resolution EDS map of the elements Sc and Zr of two nanoprecipitates with diameters of ~ 10 nm (a–d) and ~ 22 nm (e–h). EDS signals from the other elements in the nanoprecipitates were too weak in the atomic resolution EDS maps to be analyzed and were deleted. The respective images were recorded from the central core position to the outer Al matrix. Both nanoprecipitates exhibit a Sc-rich core with a Zr-rich shell implying a core–shell structure for Sc and Zr. The larger diameter nanoprecipitate, Fig. 6e–h, displays a drastic size increase for the Sc-core, while the Zr-shell thickness is constant, which implies that local Sc-rich locations contribute to larger precipitate diameters.

An interesting possibility for core–shell nanoprecipitates is that controlling the thickness of each shell can be used to obtain better creep resistance and other mechanical properties at high temperatures dependent on matrix/nanoprecipitate heterophase interfaces. Increasing the thickness of a shell by additional control of the heat treatment steps and the initial composition may permit greater control over the mechanical properties of these materials at high temperatures.

Differential scanning calorimetry of Al–Si– Sc–Zr–Er–V alloys

The DSC technique is extensively used to study solidstate reactions, such as precipitation in Al-based alloys [31]. However, calorimetry alone cannot identify the exact nature of the reactions and must be supplemented with other characterization tools, such as HRTEM and APT, to interpret the reactions corresponding to the peaks of a DSC curve. Figure 7 exhibits the DSC scan of the homogenized (supersaturated solid solution) Al–Sc–Er–Zr–V–Si alloy. The thermogram displays two prominent exothermic peaks at 90 and 300 ^{o}C, which may be attributed to GP-zone formation and subsequent nucleation of Al_3Er nanoprecipitates, respectively, due to high diffusivity of the Er. Peaks involving GP and Guinier– Preston-Bagaryatsky's (GPB) zones generally appear at ~ 100 ^{o}C in precipitation-hardenable Albased alloys [31, 32]. Koch et al. [32] report the formation of GPB zones in Al-Cu-Mg–Pb at ~ 80 ^{o}C with a T4 heat treatment and at ~ 100 ^{o}C with a T6 heat treatment. Similarly, Smith [33] demonstrated the formation of GP-zones at 110 ^{o}C during DSC analyses of a solution heat-treated 2124 aluminum alloy. To date, no evidence of GP-zones has been reported for the Al–Sc alloys, but the addition of Er, Zr, V and Si may cause the formation of GP-zones in the current alloy [34]. Erbium-rich Al_3(Er, Sc) nanoprecipitate is anticipated to nucleate first, because Er is the fastest diffusing species among all the alloying elements [35]. Hence, the second exotherm at 300 ^{o}C should correspond to Al_3(Er, Sc) nanoprecipitation. Additional precipitation peaks could not be resolved during DSC experiments, possibly due to the slower precipitation kinetics of Zr and V.

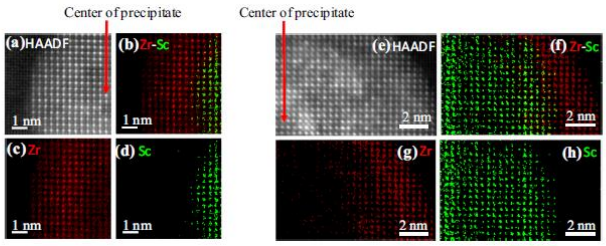

Figure 6 HAADF images and their respective atomic resolution EDS maps of Sc and Zr in a–d ~ 10 nm diameter Al_3(Sc, Zr, Er, V) nanoprecipitate and e–h ~ 22 nm diameter nanoprecipitate.

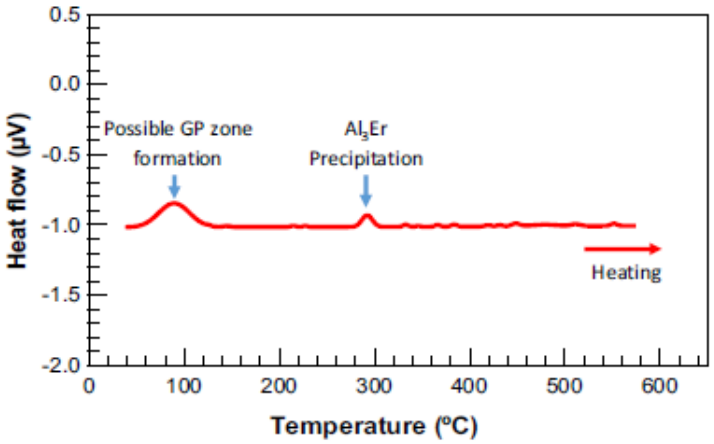

Figure 7 Differential scanning calorimetry (DSC) of a homogenized (640 ^{o}C for 4 h) Al–Sc–Er–Zr–V–Si alloy heated from 40 to 600 ^{o}C at a scan rate of 20 ^{o}C/min. The peak at 90 ^{o}C indicates a possible sign for GP-zone formation during this temperature increase.

Evolution of structural defects in Al–Si–Sc– Zr–Er–V alloys

To better understand the DSC peak observed at 90 ^{o}C, the overaged Al–Si–Sc–Zr–Er–V alloy was investigated using HRTEM and HAADF-STEM. Figure 8a and b displays TEM images of the Al–Si–Sc– Zr–Er–V alloy viewed along the [110] zone axis. The matrix contains a high density of linear distortions (marked in red), oriented mainly in two distinct planes, (111) and (111). These linear distortions have varied thicknesses ranging from 0.4 to 2.7 nm, that is, 1 to 11 atomic planes. HAADF-STEM was performed on two different linear distortions, Figs. 9 and 10, viewed along the [110] zones axis. Linear distortions are more difficult to distinguish in HAADF-STEM images because they are less sensitive to diffraction contrast [36]. Figure 9a exhibits a linear distortion, indicated by a white box. And the center of the distortion is labeled with a red arrow. After image filtering and contrast changes, the resulting image, Fig. 9b, displays two distinct atomic planes, which are slightly displaced from each other. The original Al (f.c.c.) matrix is seen in the upper left-hand corner of Fig. 9b, which can be compared to the central distorted region. There is also a slight contrast change between the two different adjacent atomic planes, which could be an indication of the difference in atomic numbers between the matrix Al atoms and adjacent solute atoms. These features do not represent a fully developed GP-zone but perhaps a preliminary cluster formation composed of remnant solid-solution elements in the f.c.c. matrix. Further local composition analyses of these clusters need to be performed to obtain conclusive evidence of the elemental character of these features.

The Fourier filtered image of the (111) plane and fast Fourier transform (FFT) of the white highlighted region are also displayed in Fig. 9b and c, respectively. The Fourier filtered image exhibits dislocations (circled in white) on either side of the feature marking the start and finish points of the structural defect. An FFT of the same region indicates some matrix distortion in the local region exhibited by the observed diagonal-band streaking of the FFT image, but a fully developed stacking fault is not present.

Evidence of atomic cluster formation has been observed in naturally aged Al-Cu alloys, where STEM was employed to indicate contrast differences of Cu atomic layers in a pure Al matrix [18]. They were labeled as Cu clusters, which developed along the (111) and (111) planes within the local regions of quenched-in dislocations, i.e., an indication of low-energy- barriers for nucleation and growth of nanoprecipitates. Particularly for Al–1.74 at% Cu alloys, aged at 165 ^{o}C for 8 h, these clusters would develop into full GPII-zones [18, 37]. It is possible that the same mechanism of cluster formation may be applicable for Al–Er–Sc–Zr–V–Si alloys. However, the lack of Z-contrast in the HAADF-STEM images does not support the formation of Er-, Sc- or Zr-rich GP-zones or clusters since the differences in atomic numbers between these elements and Al matrix should result in distinguishable contrast differences. Silicon, on the other hand, is known to contribute to the accelerated precipitation in Al–Sc alloys, and it could very well be located within the structural defects observed in Figs. 8 and 9 [8]. However, the contrast differences in these images are difficult to distinguish with the low atomic number differences between Si and Al. Accordingly, a HAADF-STEM image of a more developed structural defect and its corresponding FFT are displayed in Fig. 10 Additional spots in the FFT (marked by red arrows in the diffraction pattern inset of Fig. 10a) confirm the presence of a stacking fault (SF). The same method has been employed to demonstrate SFs and twining in nano-crystalline pure Al [38]. Coupled with solute atoms adjacent to Al atoms, the SF is more clearly visible in Fig. 10b after low-pass filtering of the image labeled in white. This could be the transition from clusters to GP-zones due to the distinct layering and SF observation in the atomic planes. In Al-Zn-Mg alloys, similar GP(II) zones have been found using HRTEM and electron diffraction [19]. The thickness of these GP(II)-zones ranges from 1.5 to 3 nm, and they are claimed to be precursors to η’ metastable-precipitates in Al-Zn-Mg alloys

[19]. Hence, the structural defects found herein in Al–Sc–Zr–Er–V–Si alloys could be precursors to the observed spherical nanoprecipitates. Another mechanism that can be proposed is that these defects are just SFs, without any solute segregation, and could become nucleation points for nanoprecipitates during the overaging treatment.

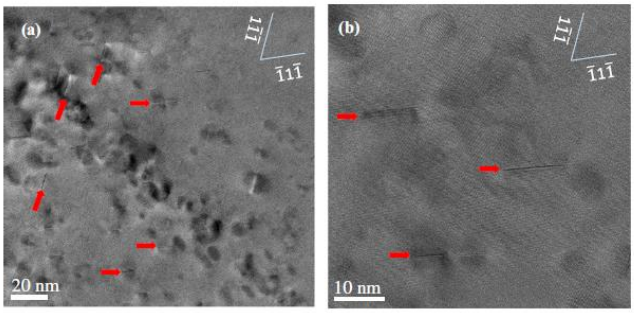

Figure 8 a Low- and b high-magnification HRTEM images of overaged Al–Er–Sc–Zr–V–Si alloy recorded along the [110] zone axis, containing multiple linear distortions aligned along the edges of the (111) and (111) planes. Some of these linear distortions are marked with red arrows.

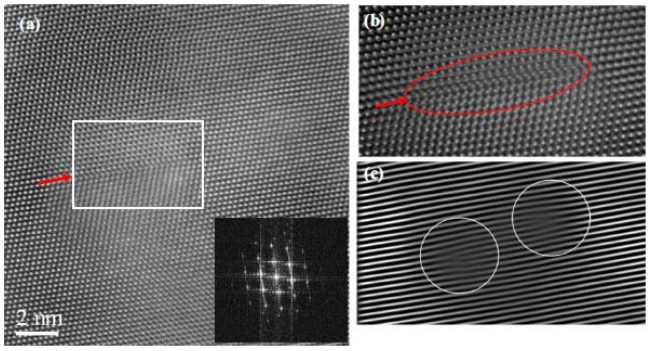

Figure 9 a A typical HAADF-STEM image of a structural defect including a fast Fourier transform of the region in the rectangular box delineated by solid white lines, exhibiting some diagonal streaking caused by distortions in the Al (f.c.c.) matrix—see inset pattern in the lower right-hand corner. b A low-pass filtered image of the region marked by rectangular box in a, displaying some solute atoms, which are displaced relative to Al (f.c.c.) matrix atoms. c Fourier masked image of the same region in b, displaying dislocations (circled in white) on either side of the cluster.

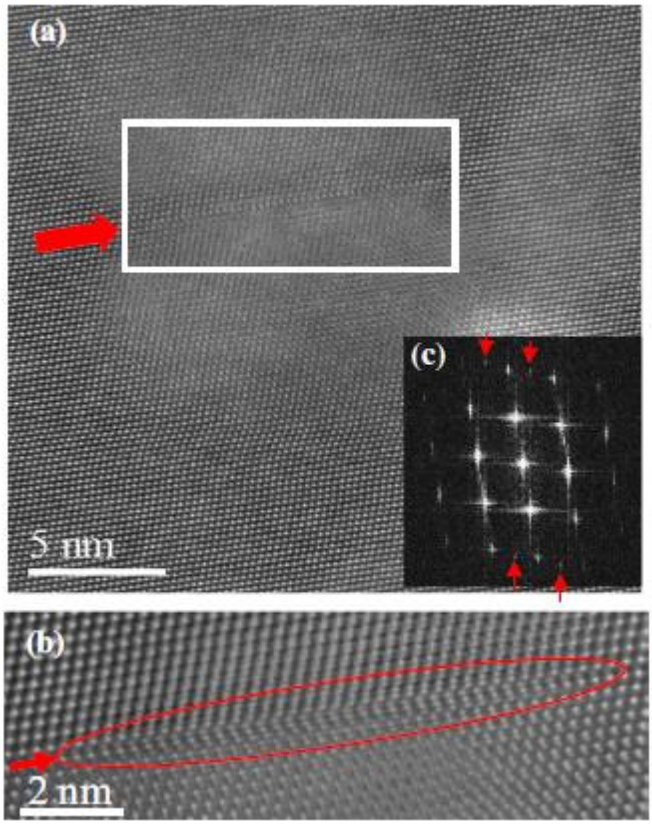

Figure 10 a HAADF-STEM image of a more developed structural defect within the rectangular box demarcated by solid white lines. b A low-pass filtered image of the region in a indicated by the rectangular box, exhibiting a stacking fault. c FFT of a exhibits extra diffraction spots indicated by red arrows, confirming the presence of a stacking fault.

Evolution of structural defects into spherical nanoprecipitates

Based on the above observations, the evolution of spherical Al_3(Sc, Zr, Er, V) nanoprecipitates formed upon aging are summarized as follows. During the casting and homogenization treatment (640 ^{o}C for 4 h), quenched-in dislocations are introduced resulting in the formation of low-energy barrier nucleation points for precipitates during the later stages. Figures 11a and b display low- and high-magnification TEM images of the cast alloy after the homogenization heat treatment, respectively. Figure 11a displays a significant density of quenched-in dislocations after the homogenization heat treatment. No evidence of similar structural defect formation in the homogenized alloy is detected, Fig. 11b; hence, these defects do not form during the casting or quenching process. Rather, they must have formed during the aging treatment, which is supported by the DSC results in Fig. 7.

The images in Fig. 12 summarize the steps involved in the morphological evolution of the nanoprecipitates. The structural defects observed in Fig. 10a reduce the nucleation barriers for cluster formation. A range of thicknesses of these defects is observed, from a few atomic layers to thicker clusters or GP-zones, where fully developed stacking faults are present. Based on the DSC measurements, Fig. 7, the clusters form at ~ 90 ^{o}C. Both these features most likely contain elements with high diffusivities and low Z-contrast, such as Si, forming the cores of the stable nanoprecipitates; further compositional analyses are required to confirm this hypothesis. The primary heat treatment at 350 ^{o}C for 16 h initiates the formation of the Er- and Sc-rich shells. These shells encapsulate the nearby clusters or GP-zones, and this may be the initiation step in the development of spherical

nanoprecipitates. During the secondary heat treatment at 450 ^{o}C for 24 h, Zr- and V-rich shells complete the nanoprecipitate morphology. Local V solute concentrations may, however, have been too small for the successful development of shells. Interestingly, the structural defects, clusters, GP-zones and nanoprecipitates are all present in the same aged alloy. Due to the dendritic nature of the cast alloy, some local regions may not have had sufficiently high concentrations of solute atoms for GPzones to develop fully into nanoprecipitates [10].

This is the first time that the evolution of nanoprecipitates in Al–Er–Sc–Zr–V–Si alloys has been tracked from solute atoms to fully spherical nanoprecipitates. It appears, from the archival literature and the observations made in the present study, that nanoprecipitate formation and growth can be related to known nanoprecipitate evolution mechanisms in Al-Cu and Al-Zn-Mg alloys.

Summary and conclusions

The crystal structure and morphological evolution of core–shell nanoprecipitates were investigated in an overaged Al–Sc–Er–Zr–V–Si high-temperature cast alloy. The main observations are summarized as follows:

1. STEM-EDS analyses (Figs. 2 and 5) exhibit distinct layers of Zr-enriched region at the outer shell of the core shell nanoprecipitates, while the center of the core is composed of randomly distributed Er- and Sc-enriched regions. The outermost shell does not exhibit any traces of V, instead V is distributed in the Al matrix for the particular nanoprecipitate investigated. The crystal structure of the nanoprecipitates is consistent with the $L1_2$-ordered structure where the structure was detected to consist of two distinct atomic layers (Fig. 4). One layer was composed mainly of Al atoms, whereas the adjacent layer contained heavier atomic elements (Er, Sc, Zr, V). Furthermore, the $L1_2$-ordered superlattice was observed for the complete cross section of the nanoprecipitates even with the changes in solute atoms (Fig. 3).

2. The evolution of Al_3(Sc, Zr, Er, V) nanoprecipitates from structural defects to linear clusters to GP-zones to spherical nanoprecipitates is proposed, and the concomitant microstructural evidence is presented (Figs. 7, 8, 9, 10, 11). However, the cluster and GP-zone stages and formation of these features could not be fully confirmed due to the difficulty of high fidelity elemental analyses using the HAADF-STEM technique. All of these features were observed in the same aged alloy sample due to fluctuations in the local solute concentrations resulting from macrosegregation, which is a result of the dendritic nature of the cast alloy. Dislocations pairs were also observed on either side of the structural defects similar to stacking faults in f.c.c, alloys (Fig. 9).

3. It can be claimed that Si, with high diffusivity and low Z-contrast, can be responsible for the formation of these clusters and later, GP-zones. Thicker layers of the structural defects could be GP-zones, which could serve as the precursors for the spherical nanoprecipitates (Fig. 12c).

4. Herein, the two-stage heat treatment permitted the remainder of Er, Sc and Zr atoms to form a shell structure, resulting in a spherical morphology of the final nanoprecipitates (Fig. 5). Due to dendritic segregation during casting, local V depleted regions did not permit the formation of a complete V shell at the matrix/precipitate heterophase interface of the nanoprecipitates studied (Fig. 2).

5. Further compositional analyses are required to assess the elemental makeup of these structural defects and to confirm if these are clusters or GPzones. It will be also helpful to relate the evolution of the nanoprecipitates to controlled heat treatment stages, where the evolution of each of these features could be isolated.

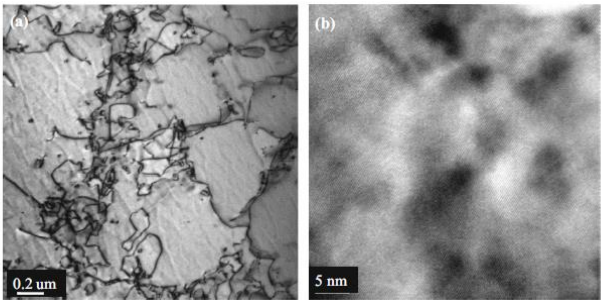

Figure 11 a TEM bright-field image of an homogenized Al–Er–Sc–Zr–V–Si alloy with extensive remnant quenched-in dislocations. b HRTEM of the same sample with no signs of clusters or GP-zone formation.

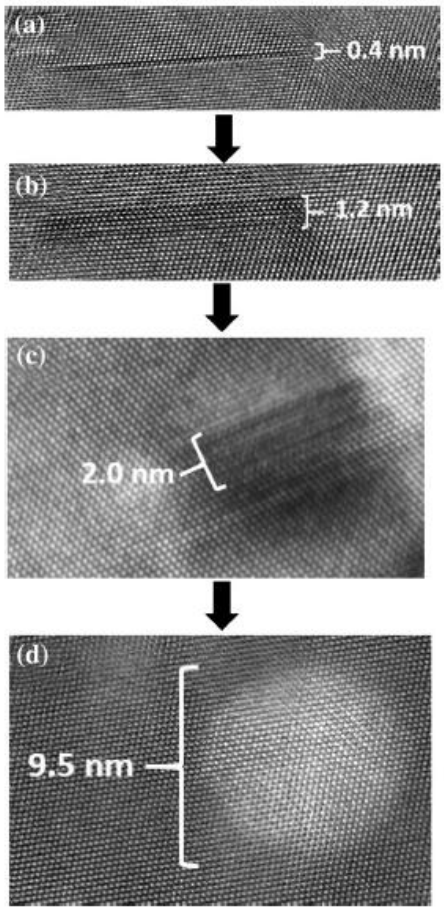

Figure 12 HRTEM images illustrating the evolution of an Al_3(Sc, Zr, Er, V) nanoprecipitate in the overaged condition from a a structural defect to b a cluster to c GP-zones, and d the last stage of growth is a spherical nanoprecipitate.

Acknowledgements

This publication was made possible by a National Priorities Research Program grant, NPRP 7-756-2-284 from the Qatar National Research Fund (a member of The Qatar Foundation); and the authors also acknowledge Spanish MINECO and FEDER under Project Number MAT2014-56116-C4-1-R for their partial financial support. R. Santamarta acknowledges the grant by the Salvador de Madariaga Program (PRX15/00549). The statements made herein are solely the responsibility of the authors. We would also like to acknowledge Microscopy and

Imaging Center at Texas A&M University, College Station for providing usage of their transmission electron microscopes and facilities.

Compliance with ethical standards

Conflict of interest DNS and DCD have financial interests in NanoAl LLC which could potentially benefit from the outcomes of this research. No conflict of interest for other authors exists for the work presented in this manuscript.

References

[1] Fuller CB, Seidman DN, Dunand DC (1999) Creep properties of coarse-grained Al(Sc) alloys at 300 _C. Scr Mater 40:691–696

[2] Novotny GM, Ardell AJ (2001) Precipitation of AlSc in binary Al–Sc alloys. Mater Sci Eng, A 318:144–154

[3] Seidman DN, Marquis EA, Dunand DC (2002) Precipitation strengthening at ambient and elevated temperatures of heat-treatable Al(Sc) alloys. Acta Mater 50:4021–4035

[4] Marquis EA, Seidman DN (2001) Nanoscale structural evolution of Al_3Sc precipitates in Al(Sc) alloys. Acta Mater 49:1909–1919

[5] Fuller CB, Seidman DN, Dunand DC (2003) Mechanical properties of Al(Sc, Zr) alloys at ambient and elevated temperatures. Acta Mater 51:4803–4814

[6] Wen SP, Gao KY, Li Y, Huang H, Nie ZR (2011) Synergetic effect of Er and Zr on the precipitation hardening of Al–Er– Zr alloy. Scr Mater 65:592–595

[7] Fuller CB, Murray JL, Seidman DN (2005) Temporal evolution of the nanostructure of Al(Sc, Zr) alloys: part I—Chemical compositions of Al(Sc, Zr) precipitates. Acta Mater 53:5401–5413

[8] Booth-Morrison C, Mao Z, Diaz M, Dunand DC, Wolverton C, Seidman DN (2012) Role of silicon in accelerating the nucleation of Al(Sc, Zr) precipitates in dilute Al–Sc–Zr alloys. Acta Mater 60:4740–4752

[9] Booth-Morrison C, Seidman DN, Dunand DC (2012) Effect of Er additions on ambient and high-temperature strength of precipitation-strengthened Al–Zr–Sc–Si alloys. Acta Mater 60:3643–3654

[10] Erdeniz D, Nasim W, Malik J, Yost AR, Park S, De Luca A, Vo NQ, Karaman I, Mansoor B, Seidman DN, Dunand DC (2017) Effect of vanadium micro-alloying on the microstructural evolution and creep behavior of Al–Er–Sc– Zr–Si alloys. Acta Mater 124:501–512

[11] Lohar AK, Mondal B, Rafaja D, Klemm V, Panigrahi SC (2009) Microstructural investigations on as-cast and annealed Al–Sc and Al–Sc–Zr alloys. Mater Charact 60:1387–1394

[12] Monachon C, Dunand DC, Seidman DN (2010) Atomicscale characterization of aluminum-based multi-shell nanoparticles created by solid-state synthesis. Small 6(16):1728–1731

[13] Monachon C, Krug ME, Seidman DN, Dunand DC (2011) Chemically and structurally complex nanoscale core/doubleshell nanoscale precipitates in an Al–Li–Sc–Yb alloy. Acta Mater 59:3398–3409

[14] Marquis EA, Seidman DN (2002) A subnanoscale study of segregation at Al/Al_3Sc interfaces. Microsc Microanal 8:1100–1101

[15] Marquis EA, Seidman DN (2004) Nanostructural evolution of Al_3Sc precipitates in an Al–Sc–Mg alloy by three-dimensional Atom-Probe microscopy. Surf Interface Anal 36:559–563

[16] Marquis EA, Seidman DN (2005) Coarsening kinetics of nanoscale Al_3Sc precipitates in an Al–Mg–Sc alloy. Acta Mater 53:4259–4268

[17] Marquis EA, Riesterer JL, Seidman DN, Larson DJ (2006) Analysis of Mg segregation at Al/Al_3Sc interfaces by atomprobe tomography. Microsc Microanal 12:914

[18] Fallah V, Korinek A, Ofori-Opoku N, Provatas N, Esmaeili S (2013) Atomistic investigation of clustering phenomenon in the Al–Cu system: three-dimensional phase-field crystal simulation and HRTEM/HTEM characterization. Acta Mater 61:6372–6386

[19] Berg LK, Gjønnes J, Hansen V, Li XZ, Knutson-Wedel M, Waterloo G, Schryvers D, Wallenberg LR (2001) GP-zones in Al–Zn–Mg alloys and their role in artificial aging. Acta Mater 49:3443–3451
[20] Deng Y, Yin Z, Zhao K, Duan J, He Z (2012) Effects of Sc and Zr microalloying additions on the microstructure and mechanical properties of new Al–Zn–Mg alloys. J Alloys Compd 530:71–80
[21] Marump T, Fujikawa S, Hirono K (1973) Diffusion of zirconium in aluminum. J Jpn Inst Met 23:17
[22] Fujikawa S (1997) Impurity diffusion of scandium in aluminium. Diffus Def Data A 115:143–147
[23] van Dalen ME, Karnesky RA, Cabotaje JR, Dunand DC, Seidman DN (2009) Erbium and ytterbium solubilities and diffusivities in aluminum as determined by nanoscale characterization of precipitates. Acta Mater 57:4081
[24] Karnesky RA, Dunand DC, Seidman DN (2009) Evolution of nanoscale precipitates in Al microalloyed with Sc and Er. Acta Mater 57:4022–4031
[25] Knipling KE, Dunand DC, Seidman DN (2006) Criteria for developing castable, creep-resistant aluminum-based alloys—a review. Int J Mater Res 97:246–265
[26] Hong T, Watson-Yang TJ, Freeman AJ, Oguchi T, Xu J (1990) Crystal structure, phase stability, and electronic structure of Ti–Al intermetallics. Phys Rev B, Am Phys Soc 41:12462–12467
[27] Lupini AR, Pennycook SJ (2003) Localization in elastic and inelastic scattering. Ultramicroscopy 96:313–322
[28] Van den Broek W, Rosenauer A, Goris B, Martinez GT, Bals S, Van Aert S, Van Dyck D (2012) Ultramicroscopy 116:8–12
[29] LeClaire AD, Lidiard AB (1956) Correlation effects in diffusion in crystals. Philos Mag 1(1956):518–527
[30] Alnatt AR, Lidiard AB (1993) Atomic transport in solids, vol 99. Cambridge University Press, Cambridge, p 787
[31] Starink MJ (2004) The analysis of Al-based alloys by calorimetry: quantitative analysis of reactions and reaction kinetics. Int Mater Rev 49:191–226
[32] Koch S, Abad MD, Renhart S, Antrekowitsch H, Hosemann P (2015) A high temperature nanoindentation study of Al– Cu wrought alloy. Mater Sci Eng, A 644:218–224
[33] Smith GW (1998) Precipitation kinetics in solutionized aluminum alloy 2124: determination by scanning and isothermal calorimetry. Thermochim Acta 317:7–23
[34] Kaiser MS (2013) Thermal analysis and kinetics of the precipitation in wrought Al–Mg, Al–Mg–Sc and Al–Mg– Sc–Me (Me = Zr, Ti) alloys. Iran J Mater Sci Eng 10:1–11
[35] van Dalen ME, Karnesky RA, Cabotaje JR, Dunand DC, Seidman DN (2009) Erbium and ytterbium solubilities and diffusivities in aluminum as determined by nanoscale characterization of precipitates. Acta Mater 57:4081–4089
[36] Pennycook SJ (1992) Z-contrast transmission electron microscopy: direct atomic imaging of materials. Annu Rev Mater Sci 22:171
[37] Biswas A, Siegel DJ, Wolverton C, Seidman DN (2011) Precipitates in Al–Cu alloys revisited: atom-probe tomographic experiments and first-principles calculations of compositional evolution and interfacial segregation. Acta Mater 59:6187–6204
[38] Chen M, Ma E, Hemker KJ, Sheng H, Wang Y, Cheng X (2003) Deformation twinning in nanocrystalline aluminum. Science 300:1275–1277